Multipath in automotive MIMO SAR imaging

Marco Manzoni, *Member, IEEE,* Stefano Tebaldini, *Senior Member, IEEE,*
Andrea Virgilio Monti-Guarnieri, *Senior Member, IEEE,* and Claudio Maria Prati

***Abstract*—This paper discusses the effect of multipath in automotive radar imaging under different sensor configurations. The study is motivated by the fact that radar technologies are becoming indispensable in the automotive scenario. Many applications such as collision avoidance systems, assisted parking, and driving assistance systems take advantage of radar technologies to accomplish their task. However, one of the main concerns about automotive radars is the possibility of detecting false targets due to multiple signal reflections. In this paper, we show how different sensor layouts experience multipath differently. In particular, we demonstrate that with Multiple-Input Multiple-Output (MIMO) radars, what really matters is the physical positions of the transmitting and receiving antennas. The monostatic/bistatic equivalent configurations cannot be used to design a system and to simulate an acquisition in the presence of multipath. We also demonstrate how vehicle-based MIMO-Synthetic Aperture Radar (MIMO-SAR) imaging can generate a bi-dimensional aperture which significantly reduces multipath effects in the focused image, avoiding the detection of false targets. All the theoretical analyses are supported by several simulations where different sensor layouts are tested, and the capability of MIMO-SAR to reject multipath is validated.**

***Index Terms*—radar; SAR; automotive; MIMO; multipath; double bounce; ghost targets**

I. Introduction

THE capability of a vehicle to perceive the surrounding environment and to act accordingly is becoming more and more crucial in the automotive industry. Parking assistance systems are now standard technology for modern cars, and autonomous driving systems are just a few years ahead of us. All these technologies are supported by a variety of different sensors such as optical cameras, LiDAR, and radars [1], [2], [3].

This paper focuses on radar sensors. Such devices are particularly attractive for the automotive industry since they can provide their own illumination to the scene. Being able to control the illumination allows for flexibility in term of spatial resolution and permit day and night imaging of the environment. Radars operating at microwave are also not particularly sensitive to fog, rain, and snow: three typical environmental scenarios that create troubles for LiDAR and cameras [4].

Conventionally, automotive radar imaging is done using Multiple-Input Multiple-Output (MIMO) architectures to generate a virtual array that achieves some angular resolution. Such resolution is bounded by the length of the virtual array and could be in the order of tens of degrees [5], [6].

All the authors are with the Department of Electronics Information and Bioengineering, Politecnico di Milano, Milano, IT, 20133 Italy e-mail: name.surname@polimi.it.

Manuscript received September 16, 2022; revised November 9, 2022.

The research interest in the field of radars for automotive applications is vivid. New sensors are developed every year with a higher number of channels, higher bandwidth, and capability to exploit different polarizations, all in a cheaper and smaller form factor [7], [8], [9]. On the algorithmic side, Deep Learning approaches, assisted by the vast amount of available data, are producing encouraging results in the field of image formation [10], segmentation [11], object detection [12] and interference mitigation [13]. A comprehensive overview of high-performance automotive radar technologies are given in [14].

In the recent years the concept of automotive-based Synthetic Aperture Radar (SAR) started to emerge with the claim to solve the lack of resolution of MIMO radars. This technique, known for decades in space-borne and air-borne radar imaging, has rarely been applied in the automotive industry. SAR imaging exploits several radar pulses transmitted by a moving platform (in this case, a vehicle) to synthesize a very long array leading to a much finer resolution than conventional radar imaging [15], [16].

The most common concern about automotive radar imaging is the presence of multipath that can lead to the detection of false targets (false alarms). Without multiple reflections, when the radar transmits a pulse, the electromagnetic wave bounces over a target and reaches the receiver, where the reflected signal is recorded. In many situations, the reflected wave may not experience a single bounce (on the target itself) but two or more bounces. This scenario is typical of closed areas such as galleries or underground parking spots, but also urban environments where guardrails, pedestrians, buildings and other vehicles are present in the scene.

Several works describe the effect of multipath in the automotive framework. A comprehensive mathematical description of the problem is presented in both [17] and [18]. The same analysis, but for Single-Input Single-output (SISO) Frequency Modulated Continuous Waves (FMCW) radars has been carried out in [19]. In [20] a full physics propagation analysis has been performed through electromagnetic modeling and simulations. A polarimetric automotive radar has been exploited in [21] to understand the multipath effect with different polarizations and laboratory tests have been carried out.

In all these works, however, there is no mention of the influence of the geometric configuration of the radar's antenna on the multipath. A MIMO array, in fact, can be proven to be equivalent to a monostatic (SISO) or bistatic (SIMO) array if there are no multiple reflections. One could be tempted to simulate the SISO or SIMO configuration, assuming that the multipath will behave equivalently in the focussed image. In this paper, we demonstrate how the MIMO, SIMO, and SISO configurations which are normally considered equivalent, generate different focussed images in the presence of multiple reflections. In other words, the actual arrangements of the transmitting and receiving antennas must be considered when designing and simulating automotive radar systems. If not taken into account, this could lead to errors in computer simulation software [22] and potentially to the design and deployment of dangerous devices.

We then proceed by assessing the effect of multipath on MIMO-SAR images. We show how ghost targets can be partially suppressed by jointly exploiting a MIMO array and SAR processing.

In Section II the geometry of the problem is explained, and the signal model is detailed with particular attention to the SIMO and SISO equivalences.

Section III is dedicated to the formal analysis of the signal received from multiple reflections. In the same section, a theoretical analysis of SISO, SIMO, and MIMO systems is derived to understand where the ghost target will appear in the focused image.

Section IV is dedicated to single-channel and multi-channel automotive SAR. It is demonstrated how MIMO-SAR, if correctly implemented, reduces the effect of multipath and in particular, of the ghost targets due to double bounces.

Section V will show the results of the numerical simulations and finally, in Section VI the conclusions are drawn.

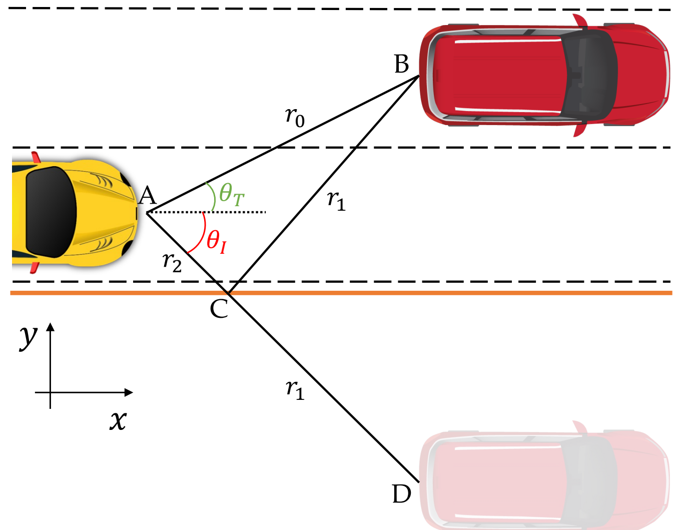

Fig. 1: Geometry of the simulated environment. The scene is typical of urban and extra-urban environments. The yellow car has a front-looking radar, the red car is a target in the opposite driveway and the transparent red car is the image target. The reflective surface is depicted in orange.

TABLE I: Propagation paths. The letter for each point is depicted in Figure 1

Path 1	A → B → A	Direct path
Path 2	A → B → C → A	First double bounce
Path 3	A → C → B → A	Second double bounce
Path 4	A → C → B → C → A	Triple bounce

II. Acquisition geometry and signal model

In this section, we start by describing the system geometry at a high level fixing the notation that will be used throughout the paper. Then, we will provide the signal model of the received signal by a MIMO radar and the SISO and SIMO equivalences.

A. Geometry of the experiment

We now focus on the geometry of the scene by defining the ranges and angles that are useful to describe the problem of the multipath. In Figure 1 a yellow car equipped with a radar travels on the roadway in the x direction. For the sake of simplicity, we consider a 2D geometry, and we freeze the scene to a particular time instant.

A target is present in the field of view of the radar. The target is depicted as a red car in the same figure. Once again, for the sake of simplicity, we will consider the car as a point target and not a distributed one. Nevertheless, the reasoning developed throughout the paper can be extended for distributed scatterers if we consider them as a collection of point targets.

On the right of the road, a reflective surface is present. These are typical conditions in urban and extra-urban environments where metallic guardrails, fences or trucks can be present. The reflective surface is depicted in Figure 1 as an orange line.

The distance between the radar and the target is denoted as r_0, and the angular position of the target with respect to the radar boresight is θ_T. A reflective surface generates an image target in the scene depicted as a light red car at the bottom of Figure 1. The angular position of the image target is denoted as θ_I. The distance from the radar to the image target is the sum of r_1 and r_2. Table I lists all the considered propagation paths.

We are now interested in going into details about the actual radar device mounted on the vehicle. As already mentioned, the car is equipped with a front-looking radar (i.e. the boresight is in front of the car). For automotive applications, the device is generally a MIMO radar with N_{TX} transmitting antennas and N_{RX} receiving ones. The total number of channels in the system is equal to $N_{ch} = N_{TX} \times N_{RX}$. The role of the array is to provide some angular resolution to the system (i.e. in the direction orthogonal to the range). There are several manufacturers of MIMO radar devices such as Texas Instruments®[23] with its 60 GHz or 76 GHz mmWave automotive radars employing up to 4 transmitting and 4 receiving antennas and up to 5 GHz of bandwidth. More sophisticated chipset are emerging in the market with up to 48 channels in transmission, and 48 channels in reception [24].

If the distance from the scatterer is large compared to the distance between the transmitting and receiving phase centers, we can approximate the total distance traveled by the electromagnetic wave as [25]:

$$|\mathbf{x}_{TX}^n - \mathbf{p}_T| + |\mathbf{x}_{RX}^m - \mathbf{p}_T| \approx 2|\mathbf{x}_V^{nm} - \mathbf{p}_T| \tag{1}$$

where $\mathbf{x}_{TX}^n$ is the position of the n^{th} transmitting element, $\mathbf{x}_{RX}^m$ is the position of the m^{th} receiving element, $\mathbf{p}_T$ is the

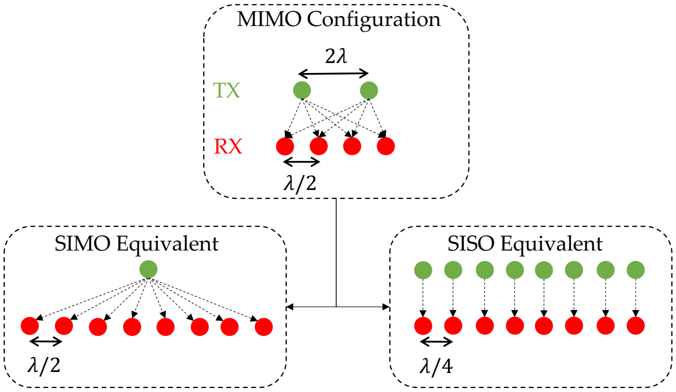

Fig. 2: An example of MIMO array with $N_{TX} = 2$ transmitting antennas and $N_{RX} = 4$ receiving ones. It can be demonstrated that this configuration, under certain hypotheses, is equivalent to a bistatic one (SIMO) or to a monostatic one (SISO).

position of the target and $\mathbf{x}_V^{nm} = \frac{1}{2}(\mathbf{x}_{TX}^n + \mathbf{x}_{RX}^m)$ is the midpoint between the TX and RX elements.

Equation 1 provides and important result: every bistatic configuration can be seen as an equivalent monostatic one composed of a virtual phase center located in the midpoint between the TX and RX element. By properly arranging the real antenna elements of the MIMO array, we can create a virtual Uniform Linear Array (ULA) with N_{ch} elements. The monostatic equivalent will be called from now on SISO, in the sense that one virtual element transmits and the same one receives the echo from the scatterer. In Figure 2 an example is given: a MIMO array with 2 transmitting elements spaced by 2λ and 4 receiving elements spaced by $\lambda/2$ can be seen as an equivalent SISO array with 8 virtual elements spaced by $\lambda/4$.

The SISO equivalent is not the only one possible. We can think of an equivalent bistatic configuration where only one antenna transmits and N_{ch} antennas receive the echo. This bistatic equivalent will be called SIMO for obvious reasons. In Figure 2 also the SIMO equivalent is depicted with receiving elements spaced by $\lambda/2$.

We remark that the transmitting and receiving real arrays can also be displaced non-uniformly, but they can still form a uniform virtual array if properly spaced.

If the MIMO array can be proven to be equal to a SISO or SIMO one, one could think that it is possible to discard completely the complicated geometry of a MIMO array and just use the simpler SISO/SIMO ones. One of the objectives of this paper is to prove that, while the SISO or SIMO equivalent configurations may be useful to understand the behavior of a complex MIMO system, they can lead to erroneous results if used for raw data simulation in the presence of multipath.

B. Signal model in absence of multipath

Let us suppose to have a generic radar where the n^{th} antenna transmits a waveform and the m^{th} receives the echo. Automotive radar systems are generally Frequency Modulated Continuous Wave (FMCW) radars where the demodulated received radar echo is multiplied complex conjugate with the transmitted one (deramping) and then range compressed with a simple Fourier Transform [26]. This operation leads to the range compressed signal $s_{nm}(t; \mathbf{p}_T)$ where t is the fast time and $\mathbf{p}_T$ is a vector indicating the position of the target in the scene.

If the transmitted pulse is assumed to be a linearly modulated chirp, we can write the model of the demodulated and range compressed signal as:

$$s_{nm}(t; \mathbf{p}_T) = \operatorname{sinc}\{B[t - t_{nm}(\mathbf{p}_T)]\} \exp\{-j2\pi f_0 t_{nm}(\mathbf{p}_T)\} \quad (2)$$

where sinc is the cardinal sine function, B is the bandwidth of the transmitted signal, $t_{nm}(\mathbf{p}_T)$ is the two-way travel time from the n^{th} transmitter to the target in $\mathbf{p}_T$ and back to the m^{th} receiving element. Notice that in Equation 2 we have also neglected an amplitude factor due to the spread loss and the Radar Cross Section (RCS) of the target.

The two-way travel time can be modeled as:

$$t_{nm}(\mathbf{p}_T) = \frac{r_n(\mathbf{p}_T) + r_m(\mathbf{p}_T)}{c} \quad (3)$$

where $r_n(\mathbf{p}_T) = |\mathbf{x}_{TX}^n - \mathbf{p}_T|$ is the distance from the n^{th} transmitter to the target, $r_m(\mathbf{p}_T) = |\mathbf{x}_{RX}^m - \mathbf{p}_T|$ is the distance from the target to the m^{th} receiver and c is the speed of light.

III. Radar Imaging in a Multipath Environment

In this section, we consider the multipath scenario represented in Figure 1. We will show that the environment is only characterized correctly when the actual layout of the MIMO array is considered, whereas the equivalent SIMO and SISO representations discussed in the previous section lead to a wrong result about the position where ghost targets appear.

A. SIMO Equivalent

In this section we focus on the equivalent bistatic configuration. We start by analyzing path 2 of Table I. The signal is transmitted by one antenna, it is reflected by the car, it bounces on the reflective surface and then it is received by the virtual array of N_{ch} elements. What we want to understand is where the ghost target will appear in the focused image. The two-way travel of Eq. 3 can be rewritten as:

$$t_{1k}(\mathbf{p}_T) = \frac{r_1(\mathbf{p}_T) + r_k(\mathbf{p}_I)}{c} \quad (4)$$

where $r_1(\mathbf{p}_T)$ is the distance from the transmitting radar ($n = 1$) to the target in $\mathbf{p}_T$ and $r_k(\mathbf{p}_I)$ is the distance from the target to the k^{th} receiving virtual element passing by the reflective surface. Notice that the former distance is exactly the same as the one from the image target in $\mathbf{p}_I$ to the k^{th} receiving element.

By combining Eq. 4 and Eq. 2 and using the plane wave approximation, we get the expression of the phase of the range compressed signal as:

$$\begin{aligned}\phi_{1k}(\mathbf{p}_T) &= -2\pi f_0 t_{1k}(\mathbf{p}_T) \\ &= -\frac{2\pi}{\lambda} r_0 - \frac{2\pi}{\lambda}[r_1 + r_2 - k\Delta_V \sin\theta_I]\end{aligned} \quad (5)$$

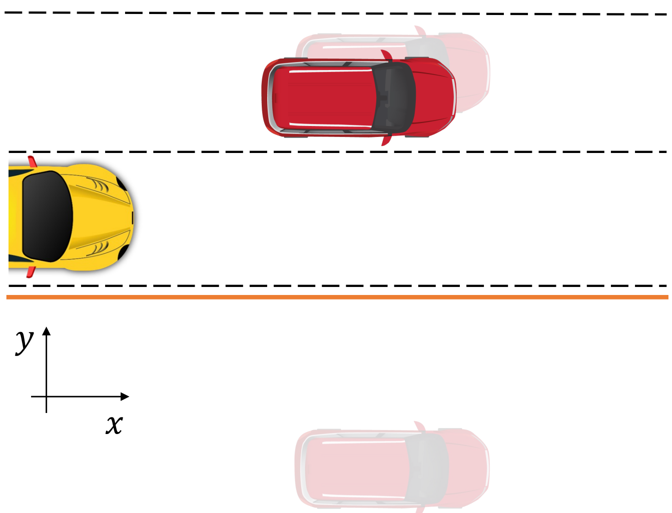

Fig. 3: Locations of the ghost targets due to double bounces in the SIMO configuration. The real target is the red car, the ghost targets are the ones in light red. In this case the ghost targets will be at the same angular position of the real and image target.

where $r_0 = r_1(\mathbf{p}_T)$ is the distance from the transmitting element to the target, $r_1 + r_2$ is the distance from the image target to the center of the receiving array and θ_I is the angular position of the image target as shown in Figure 1.

It is immediate to see that Eq. 5 is a linear phase describing a spatial sinusoid with frequency:

$$f_s = \frac{\sin\theta_I}{\lambda} \tag{6}$$

This equation relates the spatial frequency excited on the array with the angular position of the target (θ_I). Equation 6 also implicitly suggests a way to focus an image, which is a simple Fourier Transform along the channel. Notice that this works just when the phase is approximately linear. If this is not the case other algorithms can be used to focus the image such as the Time Domain Back Projection (TDBP) that will be used in the result section of this paper. If we call β the angle at which the ghost target will appear, we can state that, in this scenario, $\beta = \theta_I$. The same exact reasoning can be done with Path 3 and 4 in Table I. In general, with the SIMO configuration, the angular position at which the ghost target appears depends only upon the direction of arrival of the reflected wave. In Figure 3 a pictorial representation of the ghost targets due to double bounces is depicted. Notice that path 2 results in a ghost target behind the reflective surface (orange line), while path 3 induces a ghost near the real target.

It is straightforward to see that the range at which the double bounces will appear is just an average of the distances from the radar to the real target and from the radar to the image target. If we call r_G the range of the ghost target, we have:

$$r_G = \frac{r_0 + r_1 + r_2}{2} \tag{7}$$

where r_0, r_1 and r_2 are the distances depicted in Figure 1.

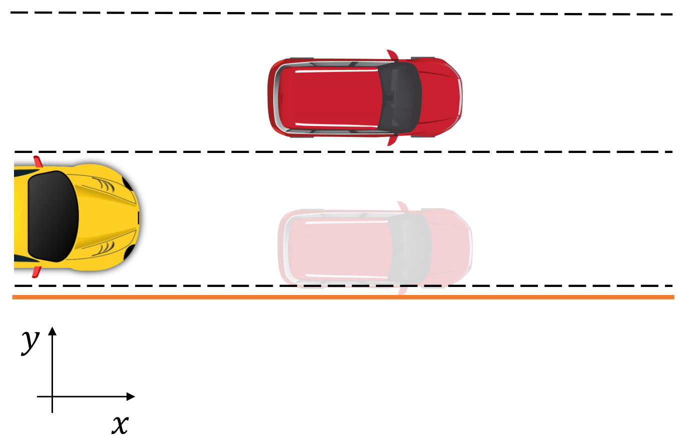

Fig. 4: Locations of the ghost targets due to double bounces in the SISO configuration. The real target is the car in red, the ghost target the one in light red. The position of the ghost target depends on both the angular position of the real and the image target. The ghost target appears right in front of the car, creating a dangerous situation.

B. SISO Equivalent

In this case the signal is transmitted by one antenna and received by only that antenna. Again, we want to understand where the ghost target will appear in the focused image. Eq. 3 can be written as:

$$t_{kk}(\mathbf{p}_T) = \frac{r_k(\mathbf{p}_T) + r_k(\mathbf{p}_I)}{c} \tag{8}$$

where the subscript kk indicates the fact that the receiving virtual antenna is the same that transmitted the waveform. Plugging again Eq. 8 into Eq. 2 and using the plane wave approximation, we get the expression of the phase of the range compressed signal:

$$\begin{aligned} &\phi_{kk}(\mathbf{p}_T) = -2\pi f_0 t_{kk}(\mathbf{p}_T) \\ &= -\frac{2\pi}{\lambda}[r_0 - k\Delta_V \sin\theta_T] - \frac{2\pi}{\lambda}[r_1 + r_2 - k\Delta_V \sin\theta_I] \end{aligned} \tag{9}$$

where this time the phase is the sum of two linear components, the first related to the angular position of the real target, the second to the angular position of the image target. The spatial frequency excited on the virtual array is now:

$$f_s = \frac{1}{\lambda}[\sin\theta_T + \sin\theta_I] \tag{10}$$

Eq. 10 suggests that the location where the ghost target will be focused depends on both the position of the real target and the image one. Indeed, this location is the angle β that satisfies the following equation:

$$\frac{2}{\lambda}\sin\beta = \frac{1}{\lambda}[\sin\theta_T + \sin\theta_I] \tag{11}$$

where the number 2 at the numerator of the first expression appears due to the monostatic nature of the virtual array. The angular position at which the multipath will be focused is no more the same position of the image target θ_I, but will be a combination of θ_T and θ_I. The same reasoning can be applied to path 3 in Table I. The triple bounce will appear in

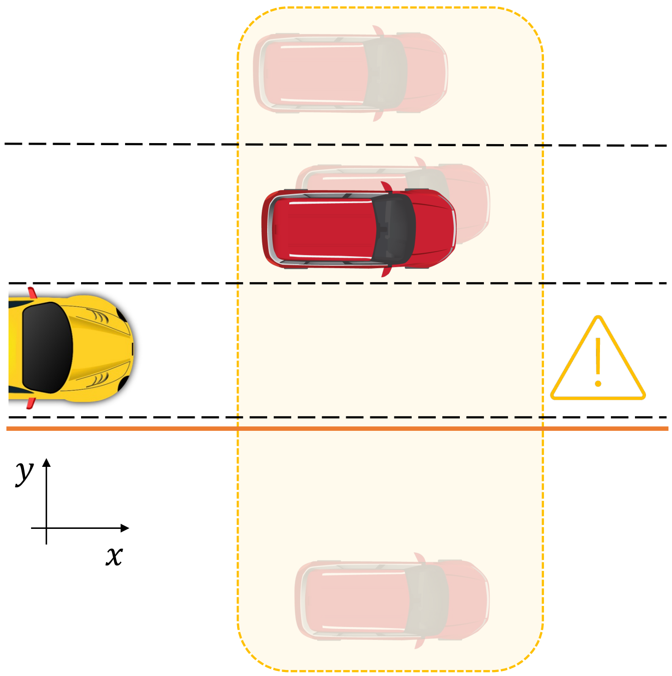

Fig. 5: Pictorial representation of the locations of the ghost targets due to double bounces in the MIMO configuration. The real target is the red car, the ghost targets are the vehicles in light red. The exact location of the ghost targets is inherently dependent on the layout of the transmitting and receiving antennas. The ghost targets will appear inside the orange box.

the position of the image target. For what concerns the range position, the same reasoning of Eq. 7 apply and the ghost targets will appear at a mid-range between the real and image targets. In Figure 4 a pictorial representation of the ghost targets due to double bounces is depicted. Notice that this time the ghost targets are in much more dangerous locations w.r.t Figure 3. One ghost target may appear in the middle of the roadway and trigger dangerous maneuvers in an autonomous driving system.

Accordingly, the analysis of this section demonstrates that the SISO and SIMO representations lead to different results in the case of multipath, therefore they cannot be taken as equivalent.

C. Multipath with a generic MIMO radar

The typical automotive radar is generally not a SISO nor a SIMO array, but a MIMO device with several transmitting and receiving antennas. It is possible to generate the same virtual array with many different real transmitting and receiving elements configurations. For example, in Figure 9a we have 4 transmitting (in red) and 8 receiving (in blue) elements uniformly spaced forming a monostatic virtual array of 32 elements (in purple). The same identical virtual array can be generated by placing the transmitting elements in couples as in Figure 10a. The virtual array will be the same, but the focused ghost targets' positions will differ. In the latter configuration, the transmitting elements are not even uniformly spaced. While an analytical analysis is not trivial, we can state as a rule of thumb that the MIMO case is a middle ground between the SISO and the SIMO one. The larger the transmitting array, the more the result will be similar to the SISO since the position of the image targets will depend tightly on the position of the transmitters. On the other hand, the smaller the transmitting array, the more the scenario will be similar to the monostatic SIMO, where the position of the ghost targets depends purely on the location of the true and image targets.

The orange box of Figure 5 delimits in a pictorial way the possible locations of the double bounces. At different antenna layouts correspond different locations of the ghost targets. As in the SISO case, there could be some potentially dangerous situations where the ghost appears in the driveway. A set of simulations with different antenna layouts are carried out in the result section of this paper.

IV. Multipath in single- and multi-channel SAR

In this section, we describe how MIMO-SAR imaging is intrinsically robust to multipath. Automotive SAR imaging is emerging in the last years thanks to its capability to generate very high-resolution images of the surrounding [27], [28]. The advantage of automotive SAR goes beyond the fact that it is intrinsically robust to double bounces. First of all, the resolution of a SAR image is only bounded by the length of the synthetic aperture exploited in the process of image focusing leading to angular resolutions well below 1 deg [27]. Moreover, focusing a SAR image requires just the radar data and the knowledge of the vehicle trajectory which can be derived using quite inexpensive devices mounted on the vehicle itself such as an Inertial Measurement Unit (IMU), a GPS, or even a simple wheel encoder (already installed by default in every vehicle) [16]. In order to obtain a fully focused SAR image, the trajectory must be known up to a fraction of the wavelength. For W-Band systems used in the automotive industry, this condition is never met even with the most sophisticated devices. For this reason, a proper residual ego-motion estimation algorithm must be envisioned in any SAR processor that aims to reach an accurate imaging of the environment [29]. It has also been proven in [30] that the computational load required by SAR focusing is easily sustainable by current high-performance automotive processing units, opening the possibility for real-time imaging of the surroundings.

Let us now focus our attention on the problem of multipath. Suppose to have a single channel monostatic radar mounted on a moving platform, in this case, a vehicle. The SAR geometry is depicted in Figure 6.

The point A in the figure is the center of the synthetic aperture and the origin of the reference system. For the sake of simplicity, we assume a short linear trajectory. In other words, we neglect phase curvature assuming that the phase is linear along the synthetic aperture. It is straightforward to write the

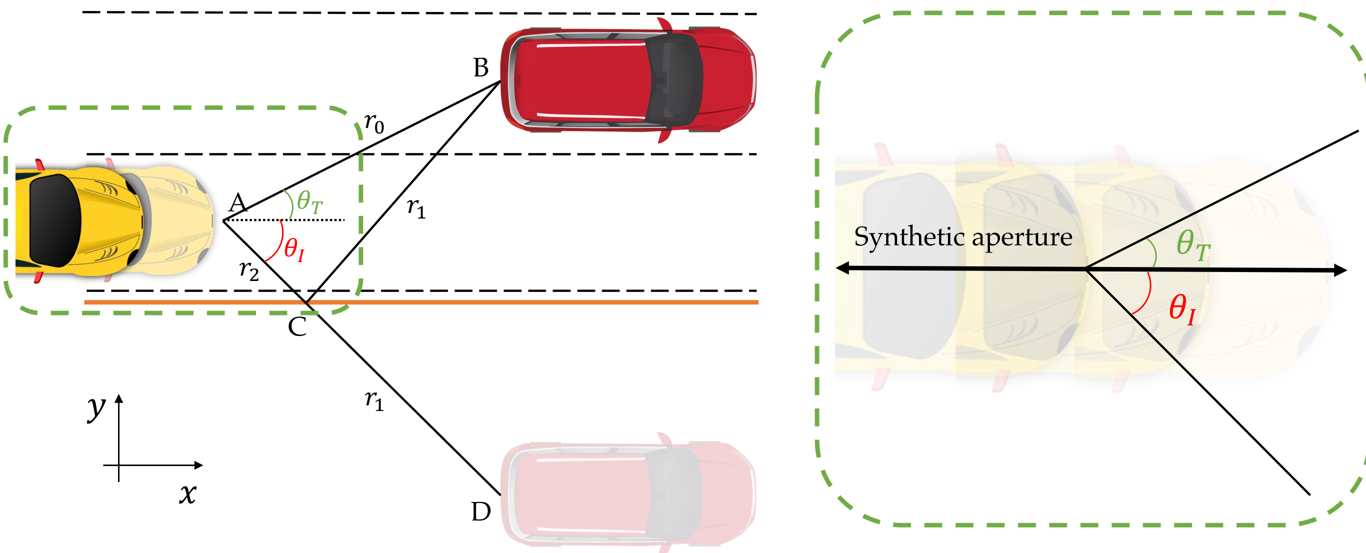

Fig. 6: Geometry of the SAR acquisition. The car is now moving in a straight path along the x direction. In the green box a zoom over the synthetic aperture is depicted.

phase history of the double bounce as done previously in Eq. 9:

$$\begin{aligned}\phi_x(\mathbf{p}_T) &= -2\pi f_0 t_x(\mathbf{p}_T) \\ &= -\frac{2\pi}{\lambda}[r_0 - x\cos\theta_T] - \frac{2\pi}{\lambda}[r_1 + r_2 - x\cos\theta_I]\end{aligned} \tag{12}$$

where x is the position of the sensor along the synthetic aperture. Notice that this time there is a cosine function, and not a sine due to the fact that the reference frame has remained the same, but the synthetic aperture is orthogonal to the virtual array which is mounted forward-looking. The spatial frequency excited on the synthetic aperture is:

$$f_s = \frac{1}{\lambda}[\cos\theta_T + \cos\theta_I] \tag{13}$$

Once again, exactly as in the SISO case, the location of the ghost target will depend on both the position of the real target and of the image one. The angular position is the angle β that satisfies:

$$\frac{2}{\lambda}\cos\beta = \frac{1}{\lambda}[\cos\theta_T + \cos\theta_I] \tag{14}$$

If we use just a single channel SAR, the system is still vulnerable to multipath exactly as the SISO virtual array. What is instead interesting is the MIMO-SAR configuration, where the virtual array is displaced orthogonal to the synthetic aperture. If we want the double bounce to be fully focused, we have to find a unique solution β that satisfies both the array spatial frequency equation *and* the SAR spatial frequency equation. It is easy to see that this is not possible for the double bounces in Eq. 10 and 13, in fact, there is no real solution to the system of equations:

$$\begin{cases}\sin\beta = \dfrac{\sin\theta_T + \sin\theta_I}{2} \\ \cos\beta = \dfrac{\cos\theta_T + \cos\theta_I}{2}\end{cases} \tag{15}$$

The virtual array tries to focus the ghost target in a location that will respect the first equation of 15, but the synthetic array tries instead to focus it in a position that will respect the second equation in 15. The result is that the SAR does not cooperate with the MIMO radar to focus the ghost target, thus the ghost target related to the double bounce is not fully focused. We remark that the same is not true for the direct path (i.e. the real target), where there is a trivial solution to the system of equations:

$$\begin{cases}\sin\beta = \sin\theta_T \\ \cos\beta = \cos\theta_T\end{cases} \tag{16}$$

which is obviously $\beta = \theta_T$. The same can be proved for the triple bounce since it resembles a direct path from the radar to an image target and back. The triple bounce is much more dangerous than the double one since it will be perfectly focused (as the main target).

The key aspect is to have a bi-dimensional aperture given by the virtual array in one direction and by the synthetic aperture in the other. The two apertures agree for what concerns the position of the single or triple bounce, but they disagree on the double bounces, leading to an unfocused impulse response. We deem that also in the case of MIMO-SAR we have to put particular attention to the actual MIMO geometry and avoid using monostatic or bistatic equivalences when simulating an acquisition and the subsequent focusing. In Section V we will show how different MIMO-SAR geometric configurations lead to different focused scenes. One last consideration must be made regarding moving targets in the scene. In an urban scenario, the targets illuminated by the radar are generally moving targets. However, it is always possible to find a suitable (inertial) reference frame in which the moving target is still, leading to a focused SAR image. An example could clarify the topic. Imagine an ego-vehicle traveling at 20 km/h, a target vehicle traveling at 5 km/h in the same direction as the ego-vehicle, and a reflective surface traveling at 5 km/h. This scenario is equivalent to one in which the target vehicle is still, the ego-vehicle travels at 15 km/h, and the reflective surface

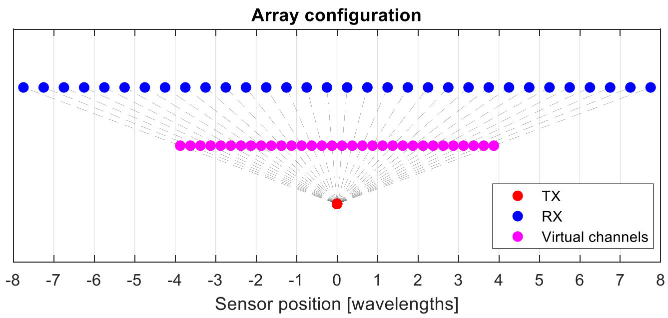

(a)

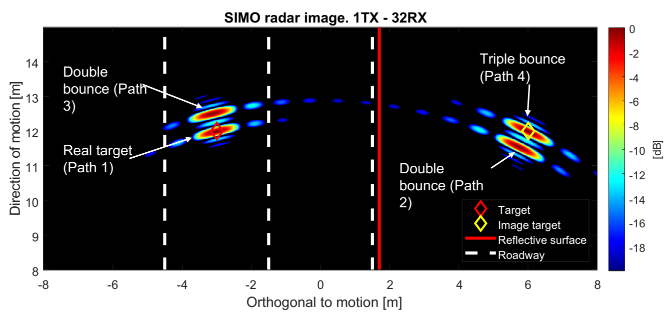

(b)

Fig. 7: (a) Real and virtual layouts of the radar antennas. In this configuration, there is one transmitting element and N_{ch} receiving one. The virtual array is the same as in Figures 8a, 9a and 10a. (b) The focused scene: the triple bounce is focused on the position of the image target, while the double bounces of path 2 and 3 are focused at the angular position θ_I and θ_T respectively.

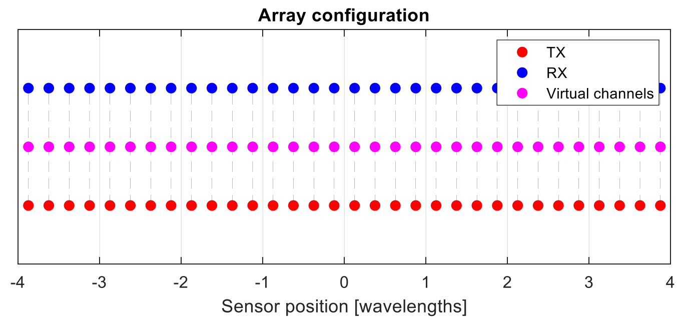

(a)

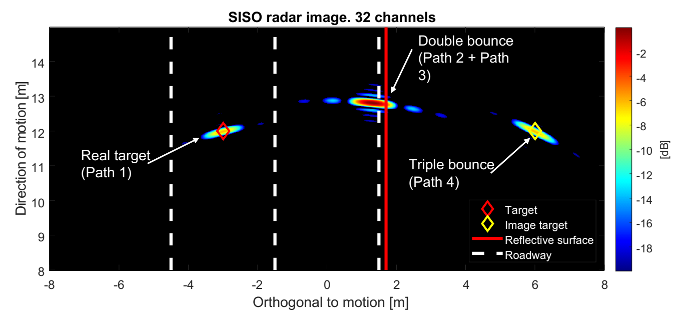

(b)

Fig. 8: (a) Real and virtual layout of the radar antennas. In this configuration, every element transmits a signal and only the same element receives the echo. The virtual array is the same as in Figures 7a, 9a and 10a. (b) The focused scene. The double bounces are focused in the same position adding up coherently. Moreover, the position of the ghost target is right in front of the car, creating a possibly dangerous scenario.

travels at 5 km/h in the opposite direction. If we assume the reflective surface to be symmetrical, all the considerations in the paper are still valid. Nevertheless, since the integration time remains the same while the relative speed decreases, the resolution the SAR provides will be lower, and the multipath mitigation capability will be reduced. In the extreme case where the ego-vehicle velocity and the target vehicle velocity are equal (in direction and magnitude), no SAR imaging can occur since the relative velocity is zero; thus no multipath suppression will take place.

V. Numerical simulations

In this section, we show the results of the simulations carried out using different sensor configurations. The simulated scenario is the one typical of the urban or extra-urban environments and it is depicted in Figure 1. A car is traveling in a straight direction on the roadway and, on the opposite carriageway there is a target. It could be an obstacle, another car or a pedestrian. At the right of the car, there is a reflective surface that generates a multipath. It could be a concrete jersey, a guardrail, a metal barrier, a wall or the side of a truck. The car is equipped with a generic SIMO/SISO/MIMO automotive radar. The parameters of the radar are listed in Table II.

In the simulation, we generate the range compressed signal as in Equation 2. The distances in Equation 3 are computed by

TABLE II: Parameters of the simulated automotive radar

Carrier frequency [f_0]	77 GHz
Signal bandwidth [B]	1 GHz
Number of virtual channels [N_{ch}]	32
Looking direction	Forward-looking
SAR aperture length	25 cm

knowing the *actual* antenna layout of the radar, the position of the real target and the position of the reflective surface. For each simulation, the received signal is the superposition of the single bounce, two double bounces and the triple bounce. All the images in this section are focused using a Time Domain Back Projection (TDBP) [31]:

$$I(\mathbf{p}) = \sum_{m,n} s_{nm}(t_{nm}(\mathbf{p});\mathbf{p}_T)\exp\left\{+j2\pi f_0 t_{nm}(\mathbf{p})\right\} \quad (17)$$

where $I(\mathbf{p})$ is the focussed image in a generic location $\mathbf{p}$, $s_{mn}(t_{nm}(\mathbf{p});\mathbf{p}_T)$ is the range compressed signal in Equation 2 evaluated at the time $t_{nm}(\mathbf{p})$, which is the total delay from the n^{th} transmitter to the pixel in $\mathbf{p}$ and back to the m^{th} receiver.

Each test has a different TX/RX antenna layout that is used for both echo simulation and image reconstruction. We highlight that, when dealing with real data, the acquisition geometry is given by the physical layout of the radar, while the geometry used for focusing can be also an equivalent

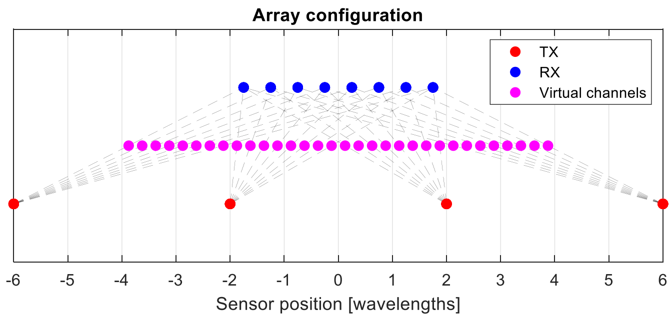

(a)

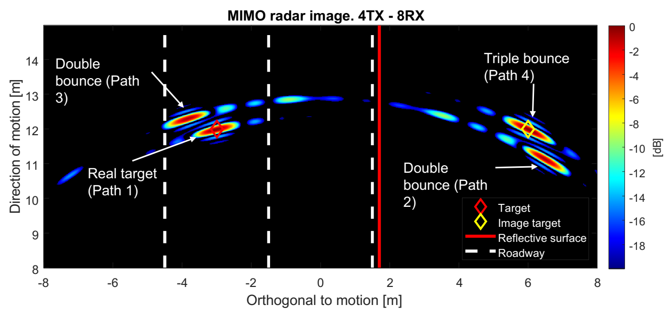

(b)

Fig. 9: (a) Real and virtual layout of the radar antennas. In this configuration, the transmitting elements are uniformly spaced. The virtual array is again the same as in Figures 7a, 8a and 10a. (b) The focused scene with double and triple bounces.

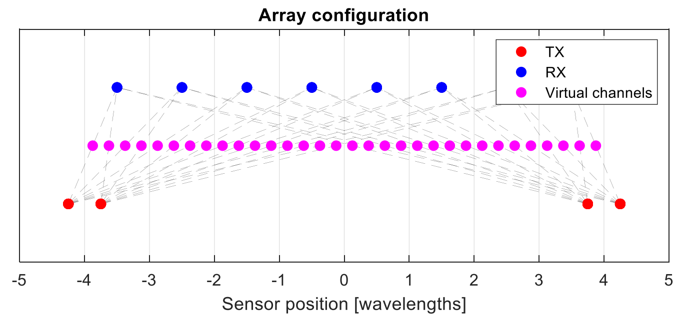

(a)

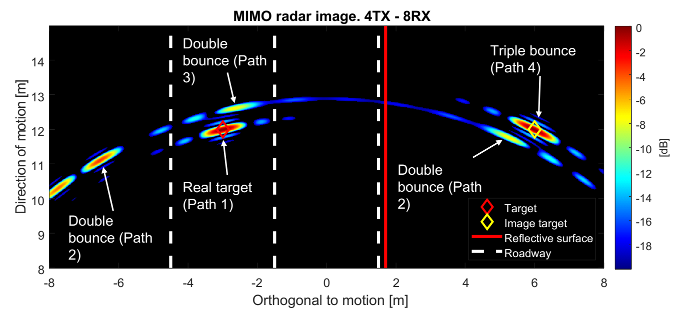

(b)

Fig. 10: (a) Real and virtual layout of the radar antennas. In this configuration the transmitting elements are not uniformly spaced, nevertheless, the virtual array is again the same as in Figures 7a, 8a and 9a. (b) The focused scene: the real target and the triple bounce are focused correctly, while the double bounces shows lower amplitudes. The double bounces are also spread at different angular positions.

SISO/SIMO one. What is important is that, when simulating the radar echo for a MIMO array, we avoid the usage of a SIMO/SISO equivalent, because the result will not be consistent.

We show that the focussed scene is tightly dependent on the layout of the radar used (SISO/SIMO/MIMO) even if all the configurations share the same monostatic or bistatic equivalent.

A. SIMO, SISO and MIMO simulations

We start from the SIMO configuration in Figure 7a where one transmitting element (in red) is present along with 32 receiving ones (in blue). The purple dots represent the equivalent virtual monostatic channels of the system. The spacing between the blue dots is $\lambda/2$ and it is set in this way to avoid ambiguities [15]. In all the simulations carried out in this paper, we considered all the paths in Table I. Figure 7b shows the focused scene. As expected the real target is exactly focused where it should be. The triple bounce signal is focused on the image target, while the two double bounces are at a range that is the average between the ranges of the real and the image target. The angular position of the focused double bounce is compatible with Eq. 6. For what concerns the amplitudes, we see that all the focussed impulse responses have the same amplitudes since there is no way in which a standard signal processing of such an array can somehow suppress the effect of multipath. In this particular scenario, however, the triple bounce and the double bounce associated with path 2 are images outside of the driveway, thus they may not cause any damage (i.e. an advanced autonomous drive system may decide to continue to drive straight since no obstacle are present on the road). We remark also that in this simulation we assumed a unitary reflection coefficient from the reflective surface. This is generally not the case in a real scenario in which double and triple bounces will be focused in a position compatible with this simulation, but with a lower amplitude due to the non-unitary reflection coefficient. A second simulation has been performed by considering a monostatic equivalent. The geometry of the array is depicted in Figure 8a. Each element transmits and only the same element receives the echo. We remark that the virtual monostatic array (the purple dots) are exactly the same as the ones in Figure 7a.

The focussed image, however, is completely different as evident by comparing Figure 7b with Figure 8b. The direct path (i.e. the real target) is correctly focused and the same is valid for the triple bounce. As predicted by Eq.10, however, the double bounce is no more focused at the same angle of the image target (yellow diamond in Figure 8b). The energy is instead concentrated at an angle between the real and the image target. In some specific scenario, the double bounce could also be focused at the center of the driveway making a potentially dangerous situation. An autonomous driving system could decide to do an emergency brake due to the presence of an obstacle on the road. Another consideration regards the

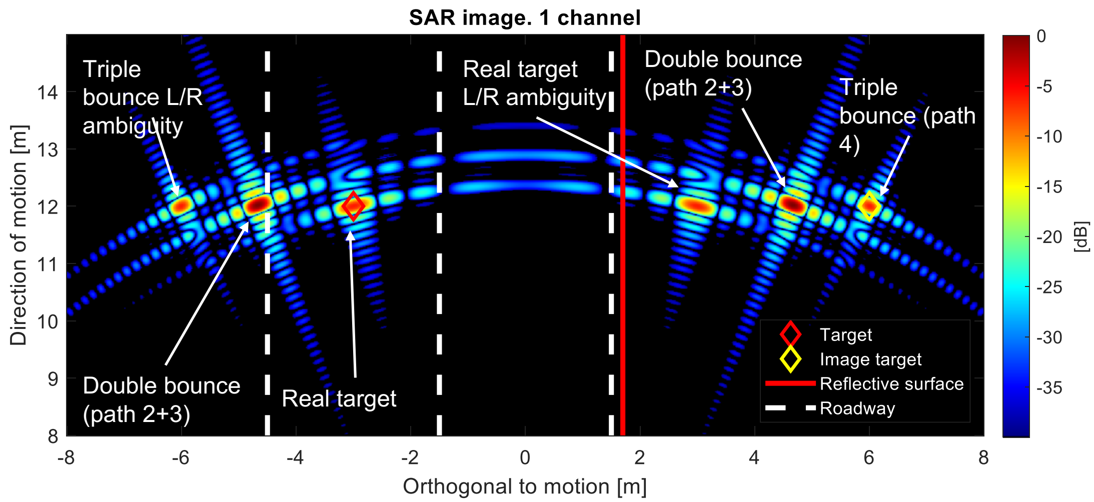

Fig. 11: Focused single channel SAR image. The system is not immune to multipath. The triple and double bounces are showing as strong ghost targets in the focused image.

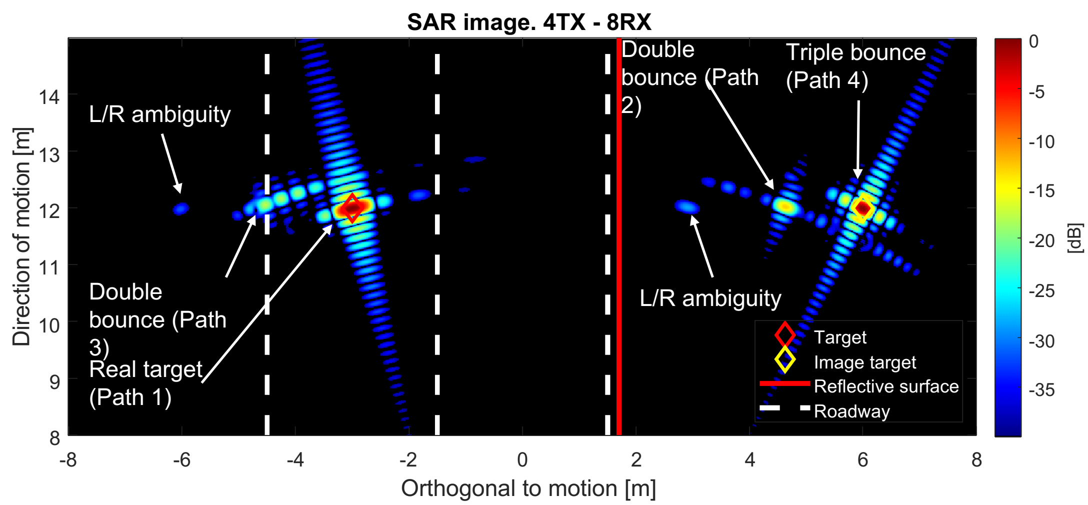

Fig. 12: Focused MIMO-SAR image. The MIMO configuration is the one in Figure 9a. The Left/Right (L/R) ambiguities are completely suppressed being 30 dB lower than the peak of the target. Also the double bounces are between 13 and 17 dB below the main peak. As expected, the triple bounce is fully focused in the position of the image target.

amplitudes of the focused impulse responses. The two double bounces from path 2 and path 3 are both reconstructed in the same position and then they sum *coherently*. This means that the amplitude of the double bounce signal is 3 dB higher w.r.t the real target signal. This could generate even more problems since this strong signal could potentially hinder the detection of some weak targets in the neighborhood, such as a pedestrian that is trying to cross the road.

The next step is to simulate a MIMO array with $N_{TX} = 4$ and $N_{RX} = 8$. We start by a simple scenario where both the transmitting and the receiving arrays are uniformly spaced. In this case the spacing between the transmitting elements in $\Delta_{TX} = 8 \times \lambda/2$ and the spacing between the receiving ones in $\Delta_{RX} = \lambda/2$. The resulting virtual monostatic array is shown in Figure 9a with purple dots. Once again it is equal to the ones in Figures 7a and 8a.

In Figure 9b it is clear that the result is very similar to the one in Figure 7a, but it is not exactly equal. The response of the double bounces are 0.7 dB lower in amplitude with respect to the previous case and moreover, their angular placement is different being at a higher angle. The range instead, remains the same. While not so different with respect to the SIMO case, this already shows that a MIMO array should never be replaced by its equivalent SIMO and SISO in a simulation. This concept is even more clear from Figures 10a and 10b. In this scenario we simulated a transmitting array where the elements are not spaced uniformly and a receiving array with elements spaced by λ. Once again the position of the virtual monostatic elements (in purple) is the same of Figures 7a,8a and 9a. The focused scene, however, is radically different with respect to the previous ones. The single and triple paths targets are focused exactly where they should be, but the double

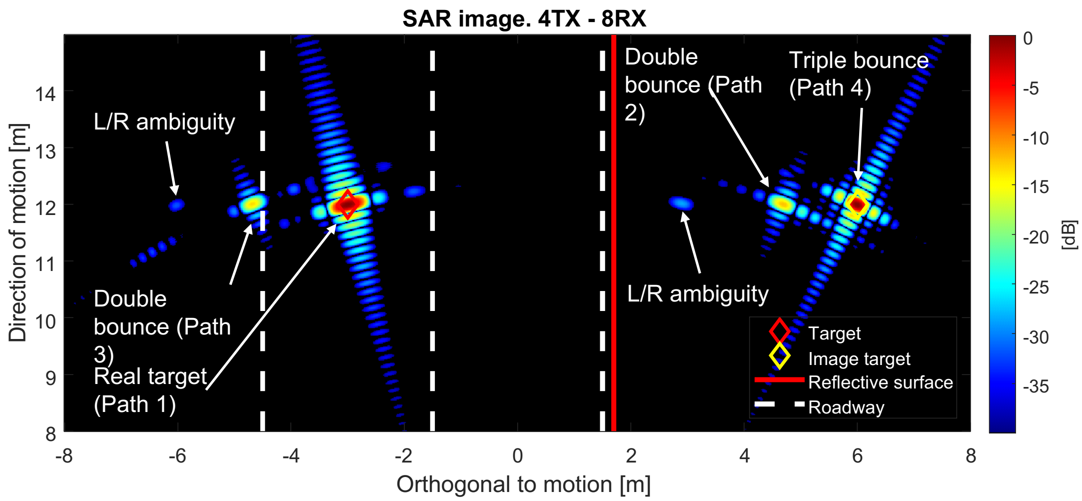

Fig. 13: Focused MIMO-SAR image. The MIMO configuration is the one in Figure 10a. The Left/Right (L/R) ambiguities are completely suppressed, being 30 dB lower than the peak of the target. Also, the double bounces are more than 15 dB below the main peak.

bounces are focused in totally different positions w.r.t. the previous cases. The double bounce of path 2 generates two responses, one to the right of the reflective surface and one outside the driveway to the left. The former is 9 dB lower w.r.t the real target, while the latter is 3 dB lower. The double bounce of path 3, instead, is reconstructed in the driveway just behind the real target almost as in Figure 7a. Its peak value is 7 dB lower than the peak associated with the real target.

B. SAR and MIMO-SAR Simulation

In this section, we propose the simulations of a complete single and multi-channel SAR system. The vehicle is now traveling is a straight path. While moving, it transmits and receives radar signals. For this simulation, we fixed the synthetic aperture length to 25 cm. The Pulse Repetition Interval (PRI) is set in such a way that the distance between two consecutive transmissions of the same antennas are spaced by $\lambda/4$ in order to avoid ambiguities [15]. The total number of slow-time samples used to form the synthetic aperture is $N_\tau = 256$. In practice, it is not required to have uniform spacing between radar transmission/receptions: once the positions of the antenna phase centers at any time instant are known, we can exploit this knowledge to focus the SAR image using a Time Domain Back Projection (TDBP). Some sophisticated imaging schemes envision the change in PRI in function of the car velocity to obtain uniform sampling in the spatial domain and a reduction in data volume.

The SAR image is focused again using a simple TDBP of all the received signals [31]. We remark that the signals received are $N_\tau \times N_{ch}$ and we back project all of them.

We started by simulating a single channel SAR ($N_{ch} = 1$). In Figure 11 the focused image is shown. In this scenario, the system is not immune to the multiple reflections, and the focused double and triple bounces appear as bright ghost targets in the scene. Moreover, the system is affected by the usual left/right ambiguity. This is an expected behavior since the aperture, in this case, is not bi-dimensional and no multipath suppression is taking place as explained in Section IV.

We continue the simulation process with a MIMO-SAR setup as in Figure 9a, but this time on a moving platform. The array is displaced in the direction orthogonal to the motion of the vehicle, leading to a bi-dimensional aperture. The focussed scene is depicted in Figure 12.

In this figure, we increased the dynamic range of the color scale to highlight the ghost targets in the image. The real target and the triple bounce are focused in the expected position and with a large improvement in angular resolution as expected by SAR processing. The two double bounces are now well below the peak of the main target: the double bounce associated with path 2 is 13dB below the main peak, while the double bounce associated with path 3 is 17 dB below. The result is expected and in accordance with the theoretical derivation in Section IV. The two apertures do not agree on where the double bounce should be focused, while they agree on the position of the single and triple bounces. This condition leads to fully focused real and image targets and to defocused double bounces.

In Figure 12 we have also highlighted the left/right (L/R) ambiguities that are typical of SAR processing. With an array displaced in the direction orthogonal to the motion, however, we are able to suppress such ambiguities. The peak values, in fact, are roughly 30 dB lower than the target peak value. The simulation proves the robustness of SAR processing to multipath and in particular its ability to suppress double bounces.

For the sake of completeness, we show also the simulation carried out by moving the MIMO configuration in Figure 10a. In Figure 13 the focused scene is depicted. It is immediate to see that it is very similar to Figure 12 despite the fact that the MIMO geometry is totally different. The reason for the similarity is that the synthetic array generated by the movement of the vehicle along a trajectory dominates the virtual array generated by the MIMO channels. The synthetic array is 25cm long, while the 32 virtual channels are just 6 cm long. This means that, for a look angle θ just a few degrees above 0, the resolution is totally given by the SAR and not by the MIMO radar. The latter serves just the purpose of suppressing the L/R ambiguities.

The results from this simulation show that the MIMO-SAR not only is able to improve the imaging reaching an extremely fine angular resolution, but it is also able to suppress the effect of multipath and in particular of the double bounce. In the non-SAR case, the triple bounce is still a problem since it will be focused exactly as the real target. However, we deem that this issue can be avoided by recognizing that the ghost target is focused behind a reflective surface. A real target should be in shadow condition, thus that reconstructed target should be immediately marked as the product of a reflection.

VI. Conclusions

In this paper, we conducted a theoretical analysis of the effect of multiple reflections in automotive radar imaging. We started by reviewing the virtual array concept and the monostatic/bistatic equivalent of any MIMO radar. We analytically proved that, in the presence of multipath, the focused image is inherently dependent upon the actual antenna layout. This demonstrates that, when designing and simulating an automotive radar system, the real antenna layout should be used (usually the MIMO one), and any equivalent representation should be carefully avoided.

In addition, we investigated the effect of multiple reflections on SAR acquisitions, particularly on MIMO-SAR images. If the MIMO array is placed in a forward-looking geometry, with the virtual array oriented in the direction orthogonal to the motion, the system forms a bi-dimensional aperture. The critical concept demonstrated in this paper is that the two apertures disagree on the angular position in which the double bounce should be focused, leading to its suppression in the focused MIMO-SAR image.

The before-mentioned analyses are validated with a simulation of the multipath environment. Several radar layouts are tested, showing how the focused image depends on the antenna layout itself. Finally, the MIMO-SAR system is also simulated with a short synthetic aperture of 25 cm. The system is robust to double bounces: they are suppressed, showing a peak amplitude between 13 and 17 dB lower than the peak associated with the real target. The system, however, is not robust with respect to triple bounces that are instead fully focused and appear as ghost targets in the SAR image.

References

[1] S. Saponara, M. S. Greco, and F. Gini, "Radar-on-Chip/in-Package in Autonomous Driving Vehicles and Intelligent Transport Systems: Opportunities and Challenges," *IEEE Signal Processing Magazine*, vol. 36, no. 5, pp. 71–84, 2019.

[2] J. Steinbaeck, C. Steger, G. Holweg, and N. Druml, "Next generation radar sensors in automotive sensor fusion systems," in *2017 Sensor Data Fusion: Trends, Solutions, Applications (SDF)*. Bonn: IEEE, Oct. 2017, pp. 1–6. [Online]. Available: http://ieeexplore.ieee.org/document/8126389/

[3] J. Kocic, N. Jovicic, and V. Drndarevic, "Sensors and Sensor Fusion in Autonomous Vehicles," in *2018 26th Telecommunications Forum (TELFOR)*. Belgrade: IEEE, Nov. 2018, pp. 420–425. [Online]. Available: https://ieeexplore.ieee.org/document/8612054/

[4] M. Kutila, P. Pyykonen, H. Holzhuter, M. Colomb, and P. Duthon, "Automotive LiDAR performance verification in fog and rain," in *2018 21st International Conference on Intelligent Transportation Systems (ITSC)*. Maui, HI: IEEE, Nov. 2018, pp. 1695–1701. [Online]. Available: https://ieeexplore.ieee.org/document/8569624/

[5] A. Durr, D. Schwarz, S. Hafner, M. Geiger, F. Roos, M. Hitzler, P. Hugler, R. Thoma, and C. Waldschmidt, "High-Resolution 160-GHz Imaging MIMO Radar Using MMICs With On-Chip Frequency Synthesizers," *IEEE Transactions on Microwave Theory and Techniques*, vol. 67, no. 9, pp. 3897–3907, Sep. 2019. [Online]. Available: https://ieeexplore.ieee.org/document/8684275/

[6] N. Touati, C. Sturm, M. Imran, A. Vanaev, M. Kohler, K. Krupinski, W. Malik, and U. Lubbert, "High Angle Resolution Automotive Radar Based on Simultaneous 12Tx Doppler-Multiplex MIMO," in *2020 17th European Radar Conference (EuRAD)*. Utrecht, Netherlands: IEEE, Jan. 2021, pp. 386–389. [Online]. Available: https://ieeexplore.ieee.org/document/9337429/

[7] L. Kannappan, S. K. Palaniswamy, M. Kanagasabai, Sachin Kumar, M. G. N. Alsath, and T. R. Rao, "Compact dual-band MIMO cubical antenna for automotive applications," *International Journal of Electronics*, pp. 1–20, Apr. 2022. [Online]. Available: https://www.tandfonline.com/doi/full/10.1080/00207217.2022.2062796

[8] C. Liang, Y. Wang, Z. Yang, X. Hu, Q. Pei, W. Gu, and L. Zhang, "Cooperative Automotive Radars with Multi-Aperture Multiplexing MIMO Sparse Array Design," *Electronics*, vol. 11, no. 8, p. 1198, Apr. 2022. [Online]. Available: https://www.mdpi.com/2079-9292/11/8/1198

[9] M. Ramesh and C. Geetha Priya, "Miniaturized four port MIMO antenna for automotive communications," *Analog Integrated Circuits and Signal Processing*, vol. 111, no. 1, pp. 25–33, Apr. 2022. [Online]. Available: https://link.springer.com/10.1007/s10470-022-01988-2

[10] J. Fuchs, M. Gardill, M. Lubke, A. Dubey, and F. Lurz, "A Machine Learning Perspective on Automotive Radar Direction of Arrival Estimation," *IEEE Access*, vol. 10, pp. 6775–6797, 2022. [Online]. Available: https://ieeexplore.ieee.org/document/9674901/

[11] J. Liu, W. Xiong, L. Bai, Y. Xia, T. Huang, W. Ouyang, and B. Zhu, "Deep Instance Segmentation with Automotive Radar Detection Points," *IEEE Transactions on Intelligent Vehicles*, pp. 1–1, 2022. [Online]. Available: https://ieeexplore.ieee.org/document/9762032/

[12] T. Wengerter, R. Perez, E. Biebl, J. Worms, and D. O'Hagan, "Simulation of Urban Automotive Radar Measurements for Deep Learning Target Detection," in *2022 IEEE Intelligent Vehicles Symposium (IV)*. Aachen, Germany: IEEE, Jun. 2022, pp. 309–314. [Online]. Available: https://ieeexplore.ieee.org/document/9827284/

[13] C. Jiang, Z. Zhou, and B. Yang, "Unsupervised Deep Interference Mitigation for Automotive Radar," in *2022 IEEE 12th Sensor Array and Multichannel Signal Processing Workshop (SAM)*. Trondheim, Norway: IEEE, Jun. 2022, pp. 296–300. [Online]. Available: https://ieeexplore.ieee.org/document/9827829/

[14] G. Hakobyan and B. Yang, "High-Performance Automotive Radar: A Review of Signal Processing Algorithms and Modulation Schemes," *IEEE Signal Processing Magazine*, vol. 36, no. 5, pp. 32–44, Sep. 2019. [Online]. Available: https://ieeexplore.ieee.org/document/8828004/

[15] S. Tebaldini, M. Manzoni, D. Tagliaferri, M. Rizzi, A. V. Monti-Guarnieri, C. M. Prati, U. Spagnolini, M. Nicoli, I. Russo, and C. Mazzucco, "Sensing the Urban Environment by Automotive SAR Imaging: Potentials and Challenges," *Remote Sensing*, vol. 14, no. 15, p. 3602, Jan. 2022, number: 15 Publisher: Multidisciplinary Digital Publishing Institute. [Online]. Available: https://www.mdpi.com/2072-4292/14/15/3602

[16] D. Tagliaferri, M. Rizzi, M. Nicoli, S. Tebaldini, I. Russo, A. V. Monti-Guarnieri, C. M. Prati, and U. Spagnolini, "Navigation-Aided Automotive SAR for High-Resolution Imaging of Driving Environments," *IEEE Access*, vol. 9, pp. 35 599–35 615, 2021. [Online]. Available: https://ieeexplore.ieee.org/document/9363205/

[17] F. Engels, M. Wintermantel, and P. Heidenreich, "Automotive MIMO radar angle estimation in the presence of multipath," in *2017 European Radar Conference (EURAD)*, Oct. 2017, pp. 82–85.

[18] A. Kamann, P. Held, F. Perras, P. Zaumseil, T. Brandmeier, and U. T. Schwarz, "Automotive Radar Multipath Propagation in Uncertain Environments," in *2018 21st International Conference on Intelligent Transportation Systems (ITSC)*, Nov. 2018, pp. 859–864, iSSN: 2153-0017.

[19] C. Liu, S. Liu, C. Zhang, Y. Huang, and H. Wang, "Multipath propagation analysis and ghost target removal for FMCW automotive radars," in *IET International Radar Conference (IET IRC 2020)*, vol. 2020, Nov. 2020, pp. 330–334.

[20] U. Chipengo, "Full Physics Simulation Study of Guardrail Radar-Returns for 77 GHz Automotive Radar Systems," *IEEE Access*, vol. 6, pp. 70 053–70 060, 2018, conference Name: IEEE Access.

[21] T. Visentin, J. Hasch, and T. Zwick, "Analysis of multipath and DOA detection using a fully polarimetric automotive radar," in *2017 European Radar Conference (EURAD)*, Oct. 2017, pp. 45–48.

[22] "Simulate Radar Ghosts Due to Multipath Return - MATLAB & Simulink - MathWorks Italia." [Online]. Available: https://it.mathworks.com/help/radar/ug/simulating-radar-ghosts-due-to-multipath.html

[23] T. I. , "Automotive mmWave Radar Sensors," Nov. 2022. [Online]. Available: https://www.ti.com/sensors/mmwave-radar/automotive/overview.html

[24] R. Arbe, "Arbe," Nov. 2022. [Online]. Available: https://arberobotics.com/

[25] J. H. G. Ender and J. Klare, "System architectures and algorithms for radar imaging by MIMO-SAR," in *2009 IEEE Radar Conference*. Pasadena, CA, USA: IEEE, 2009, pp. 1–6. [Online]. Available: http://ieeexplore.ieee.org/document/4976997/

[26] A. Meta, P. Hoogeboom, and L. P. Ligthart, "Signal Processing for FMCW SAR," *IEEE Transactions on Geoscience and Remote Sensing*, vol. 45, no. 11, pp. 3519–3532, Nov. 2007. [Online]. Available: http://ieeexplore.ieee.org/document/4373378/

[27] S. Tebaldini, M. Rizzi, M. Manzoni, A. M. Guarnieri, C. Prati, D. Tagliaferri, M. Nicoli, U. Spagnolini, I. Russo, and C. Mazzucco, "SAR imaging in automotive scenarios," in *2022 Microwave Mediterranean Symposium (MMS)*. Pizzo Calabro, Italy: IEEE, May 2022, pp. 1–5. [Online]. Available: https://ieeexplore.ieee.org/document/9825599/

[28] H. Iqbal, M. B. Sajjad, M. Mueller, and C. Waldschmidt, "SAR imaging in an automotive scenario," in *2015 IEEE 15th Mediterranean Microwave Symposium (MMS)*. Lecce, Italy: IEEE, Nov. 2015, pp. 1–4. [Online]. Available: http://ieeexplore.ieee.org/document/7375430/

[29] M. Manzoni, D. Tagliaferri, M. Rizzi, S. Tebaldini, A. V. Monti-Guarnieri, C. M. Prati, M. Nicoli, I. Russo, S. Duque, C. Mazzucco, and U. Spagnolini, "Motion Estimation and Compensation in Automotive MIMO SAR," *arXiv:2201.10504 [eess]*, Jan. 2022, arXiv: 2201.10504. [Online]. Available: http://arxiv.org/abs/2201.10504

[30] M. Manzoni, S. Tebaldini, A. V. Monti-Guarnieri, C. M. Prati, and I. Russo, "A Comparison of Processing Schemes for Automotive MIMO SAR Imaging," *Remote Sensing*, vol. 14, no. 19, p. 4696, Sep. 2022. [Online]. Available: https://www.mdpi.com/2072-4292/14/19/4696

[31] I. G. Cumming and F. H.-c. Wong, *Digital processing of synthetic aperture radar data: algorithms and implementation*, ser. Artech House remote sensing library. Boston: Artech House, 2005, oCLC: ocm56805179.

Marco Manzoni (Member, IEEE) was born in Lecco, Italy, in 1994. He received a B.Sc. (2016), M.Sc. (2018), and Ph.D. (2022) in Telecommunication engineering from Politecnico di Milano. His research is focused on signal processing techniques for radar remote sensing, including space-borne and car-borne Synthetic Aperture Radar signal processing, water vapor estimation from space-borne Interferometric SAR measurements, and change detection. He is currently involved in the interferometric commissioning phase of the new Copernicus Sentinel-1C mission.

Stefano Tebaldini (Senior Member, IEEE) received the M.S. degree in telecommunication engineering and the Ph.D. degree from the Politecnico di Milano, in 2005 and 2009, respectively. Since 2005, he has been with the Digital Signal Processing Research Group, Politecnico di Milano, where he currently holds the position of Associate Professor.

His research activities mostly focus on Earth Observation with Synthetic Aperture Radar (SAR) and Radar design and processing. He is one of the inventors of a new technology patented by T.R.E. for the exploitation of multiple interferograms in presence of distributed scattering. He teaches courses on signal theory and remote sensing at the Politecnico di Milano. He has been involved as a key scientist in several studies by the European Space Agency (ESA) concerning the tomographic phase of BIOMASS. He was a member of the SAOCOM-CS ESA Expert Group and is currently a member of the BIOMASS MAG at ESA.

Andrea Virgilio Monti-Guarnieri (Senior Member, IEEE) received the M.Sc. degree (cum laude in electronic engineering, in 1988. He has been a Full Professor with the Dipartimento di Elettronica, Informazione e Bioingegneria, since 2017. He is the Founder of PoliMi spin-off Aresys (2003), targeting SAR, radar, and geophysics applications. He has an H index (Google) of 33, 5400 citations, received four conference awards, and holds applications for five patents. His current research interests focus on radar-based system design, calibration, MIMO, and geosynchronous SAR. He has been a reviewer of several scientific journals, Guest Editor for MPI Remote Sensing, and a member in scientific-technical committees of international workshops and symposia on Radar and Earth Observation (EO).

Claudio Maria Prati is currently a Full Professor of Telecommunications with the Electronic Department, Politecnico of Milano (POLIMI). He has chaired the Telecommunications Study Council at POLIMI. He holds five patents in the field of SAR and SAS data processing. He has been awarded three prizes from the IEEE Geoscience and Remote Sensing Society (IGARSS '89 and IGARSS '99 and best TGARSS paper 2016). He has published more than 150 papers on SAR and SAS data processing and Interferometry. He has been involved as the key scientist in several studies by the European Space Agency (ESA), the European Union (EU), the Italian National Research Council (CNR), the Italian Space Agency (ASI), and ENI-AGIP. He is the Co-Founder of Tele-Rilevamento Europa (T.R.E), a spin-off company of POLIMI that has recently become T.R.E Altamira, a CLS French group company.